International Journal of Thermal Sciences 48 (2009) 2341–2354

Contents lists available at ScienceDirect

International Journal of Thermal Sciences

journal homepage: www.elsevier.com/locate/ijts

Influence of spiky twisted tape insert on thermal fluid performances of tubular air–water bubbly flow

Shyy Woei Chang [a,*], Arthur William Lees [b,1], Hsien-Tsung Chang [c,2]

[a] Thermal Fluids Laboratory, National Kaohsiung Marine University, No. 142, Haijhuan Road, Nanzih District, Kaohsiung City 81143, Taiwan, ROC
[b] School of Engineering, Swansea University, Singleton Park, Swansea, South Wales SA2 8PP, UK
[c] Department of Marine Engineering, National Kaohsiung Marine University, No. 142, Haijhuan Road, Nanzih District, Kaohsiung City 81143,Taiwan, ROC

ARTICLE INFO

Article history:
Received 25 February 2009
Received in revised form
5 May 2009
Accepted 5 May 2009
Available online 30 May 2009

Keywords:
Spiky twisted tap insert
Air–water tubular bubbly flow
Pressure drop
Mean Nusselt number

ABSTRACT

An experimental study that comparatively examined the two-phase flow structures, pressure drops and wall-to-fluid heat transfer properties between the plain tube and the enhanced tube with the spiky twisted-tape insert (swirl tube), was performed to disclose their differential thermal-fluid performances with air–water flows. On-line and post-processed high-speed digital images of air–water two-phase phenomena in plain and swirl tubes were detected to ensure the bubbly flow pattern in plain tube and to visualize their characteristic interfacial structures. Superficial liquid Reynolds number (Re_L) and air-to-water mass flow ratio (AW), which were respectively controlled in the ranges of 5000–15,000 and 0.0004–0.01, were selected as the controlling parameters of heat transfer performances. The dispersed rising air bubbles in the plain tube and the centrifugal-force induced coherent spiral stream of coalesced bubbles in the swirl-tube core considerably modify the pressure-drop and heat-transfer performances from the single-phase conditions. Selected results of pressure-drop and heat-transfer measurements, flow images and tube-averaged void fractions detected from the plain and swirl tubes with air–water two-phase flows were cross-referenced to illustrate the mechanisms responsible for the modified thermal-fluid performance due to the spiky twisted-tape insert. Empirical heat transfer correlations which evaluate the Nusselt numbers over the developed flow regions of the plain and swirl tubes with air–water two-phase flows were generated for industrial applications.

1. Introduction

Heat transfer enhancements (HTE) of single- and multi-phase flows have found various applications for optimal designs and reliable operations of components, machineries and systems involving heat exchanges. With the increased pumping power penalties, the passive HTE measures widely employ the extended heat transfer surfaces (undulant walls, ribs, pins, fins, dimples) and the mixing promoters (twisted tapes, vortex generators) to trigger favorable mechanisms for HTE. The twisted tape insert can also serve retrofit applications. The flow complexities induced by the helical pathway in a swirl duct with the twisted tape insert modify both single-phase and gas–liquid two-phase flows from the plain duct scenarios [1–25]. For single phase flow, the centrifugal force induces secondary flows in the form of vortexes which prevail over the entire swirl duct. HTE effects are generally attributed to the increased axial velocity by partitioning and blockage of the ducted flow, the fin effect of twisted tape, the elongated twisted flow path and the body-force influences through the centrifugal acceleration [1–10]. These tape-induced swirls modify the near wall velocity profile due to the various vorticity distributions in the vortex core [1]. Fluid mixings and hence the momentum/energy exchanges between the duct core and the near wall region are enhanced by introducing the tangential flow velocities as a result of centrifugal force effects. Due to the lack of fluctuating fluid mixings in laminar swirl ducts, such improved momentum and energy exchanges in the direction normal to duct wall have led the twisted tape to a very effective HTE measure. With turbulent flows, the pair of swirls in a swirl duct is characterized by rather uniform axial velocity [2] that results in large velocity and temperature gradients across the thin boundary layer and leads to augmentations of near-wall heat convection and shearing drag. For the single phase laminar and turbulent flows, Reynolds number (Re) and twist ratio (y) of the twisted tape are treated as the controlling parameters for both pressure drop and heat transfer correlations. In the circular tube [4,5] and square duct [9,10] with a twisted tape insert, sharp

* Corresponding author. Tel.: +886 7 8100888 5216; fax: +886 7 3629500.
E-mail address: swchang@mail.nkmu.edu.tw (S.W. Chang).
[1] Phone: +44 1792 205678. Email: A.W.Lees@swansea.ac.uk.
[2] Phone: +886 7 8100888 5217. Email: tufei@cm1.hinet.net.

1290-0729/$ – see front matter © 2009 Elsevier Masson SAS. All rights reserved.
doi:10.1016/j.ijthermalsci.2009.05.002

Nomenclature

English symbols

A, B	functional coefficients in heat transfer correlations
A	cross-sectional area of test tube (m^2)
AW	air-to-water mass flow ratio $= \dot{m}_G/\dot{m}_L = \chi/(1-\chi)$
C_p	specific heat of liquid (water) ($J\,kg^{-1}\,K^{-1}$)
D	inner diameter of test tube (m)
G	gravitational acceleration (ms^{-2})
k_f	thermal conductivity of liquid (water) ($W\,m^{-1}\,K^{-1}$)
$\dot{m}_G$	mass flow rate of gas phase (air) ($kg\,s^{-1}$)
$\dot{m}_L$	mass flow rate of liquid phase (water) ($kg\,s^{-1}$)
Nu	local Nusselt number $= q_f D/[(T_w - T_b)k_f]$
$\overline{Nu}_P$	mean Nusselt number for developed flow (plain tube)
$\overline{Nu}_S$	mean Nusselt number for developed flow (swirl tube)
P	axial distance of twist pitch with 180° rotation of tape (m)
Pr	Prandtl number of liquid (water) ($\mu C_p/k_f$)
ΔP_P	pressure difference between plain-tube entry and exit (mm H_2O)
ΔP_S	pressure difference between swirl-tube entry and exit (mm H_2O)
q_f	convective heat flux ($W\,m^{-2}$)
Re_L	superficial liquid (water) Reynolds number $= \rho_L U_{LS} D/\mu_L$
T_b	fluid bulk temperature (K)
T_w	wall temperature (K)
U_{GS}	gas (air) superficial velocity $= \dot{m}_G/(A\rho_G)$ ($m\,s^{-1}$)
U_{LS}	liquid (water) superficial velocity $= \dot{m}_L/(A\rho_L)$ ($m\,s^{-1}$)
x	axial location referred to flow entry as origin (m)
X	dimensionless axial location (x/D)
Y	twist ratio $(P/D) = 2$

Greek symbols

α	averaged void fraction across test tube
χ	dryness fraction $= \dot{m}_G/(\dot{m}_L + \dot{m}_G)$
ρ_G	gas (air) density ($kg\,m^{-3}$)
ρ_L	liquid (water) density ($kg\,m^{-3}$)
μ_L	liquid (water) dynamic viscosity ($kg\,m^{-1}\,s^{-1}$)
η	thermal performance index $= (\overline{Nu}_S/\overline{Nu}_P)/(\Delta P_S/\Delta P_P)$

transition from laminar to turbulent flow for pressure-drop and heat-transfer coefficients is not observed. The generalized heat transfer and pressure drop correlations for single phase flows in a swirl tube were accordingly derived [8] by inferring that the twisted tape insert inhibited the transitional jump from laminar to turbulent flow. Nevertheless, while the considerable HTE effects are generated by the centrifugal force in a laminar swirl tube due to the improved fluid mixings in the direction normal to the wall, the HTE impacts in turbulent swirl tubes fall dramatically from the laminar conditions [6,7] as the turbulent flow already inherits HTE benefits from the persisting flow fluctuations that improve momentum and energy exchanges normal to the wall. Less impact for intensifying the turbulent mixings can be achieved by fitting a smooth-walled twisted tape insert. As a result, the searches for extending *Re* ranges with considerable HTE effects for turbulent swirl ducts are continued. In this regard, a branch of research activities seeks for the compound HTE measures by combining the twisted tape with other HTE element(s) [11–13]. With augmentations in turbulent activities using the undulant tube wall [11], the twisted tape in the corrugated tube can increase heat transfer rates for single-phase flows to 1.9–9.6 times of the plain tube levels in the *Re* range of 3000–60,000. The combined turbulator, consisting of an internal twisted tape with the external tape which was spirally winded on the internal tape [12], offered the higher HTE impacts than those generated by a single twisted tape. Other attempts modified the geometries of twisted tape to utilize the separated shear layers for promoting turbulent activities in swirl ducts by devising the serrated [14] and spiky twisted-tapes [15]. The improved HTE performances achieved by modifying the geometry of the twisted tape can lead to further compound HTE benefits when these modified twisted tapes are combined with other HTE measures. In the tube with a serrated twisted-tape insert, the separated shear layers tripped at the serrated protruding edges of the twisted tape convect along with the swirls which augment heat transfers by the factors of 1.25–1.67 times over the swirl tube fitted with a smooth-walled twisted tape [14]. With the spiky twisted tape insert in a tube, the spirally arranged spikes induce swirls and trip the separated shear layers downstream these spikes that promote fluid mixings, vorticities and turbulent activities. Heat transfer levels in the tube with a spiky twisted tape insert are elevated to 1.28–2.4 times of the swirl tube with the smooth-walled twisted tape insert. The present study is a follow-up investigation to examine the HTE and pressure-drop performances in the tube with a spiky twisted tape insert for two-phase air–water flows. Due to the deformability and the compressibility of the gas phase, the flow and heat-transfer mechanisms of gas–liquid flows are further complicated from the single-phase flow conditions. No previous study is available in the literature that examines the heat transfer and pressure drop performances of a swirl tube with the spiky twisted-tape insert.

The interface and discontinuities of properties between gas and liquid phases further complicate mass-, momentum- and energy-transfers in a swirl duct. The complexities for a gas–liquid two-phase flow arise due to the interacting mechanisms at the interfaces which geometries are constantly varied and convected within the flow. These interfacing mechanisms depend on the interfacial structures and the local driving forces such as gravity, pressure gradients and centrifugal forces in swirl ducts. The interfacial structures of two-phase flows are generally characterized by the two-phase flow regimes, such as bubbly, slug and annual flows, which are conveniently specified by the superficial liquid and gas velocities for a set of predefined flow conditions. Various interfacial structures result in different transports of interfacial area concentration and void fraction. The driving forces that promote the local transport mechanisms such as the turbulent interactions and interfacial fluxes vary among two-phase systems. The interdependent effects of interfacial structures and driving forces affect the coalescence and disintegration processes for two-phase flows and therefore play the decisive role in determining the transition of two-phase regimes. Kocamustafaogullari et al. [16] examined several bubble breakup mechanisms and reported that the average pressure fluctuations generated by the liquid turbulences acting across a bubble could cause bubble distortions. Liquid turbulent structures are predominantly controlled by the liquid Reynolds number (Re_L). With low liquid velocities (low Re_L) that the liquid turbulence levels were not sufficient to trigger bubble breaks, the rates of bubble coalescence generally increased with the increase of void fraction due to the enhanced bubble–bubble interactions. For high liquid velocities (high Re_L), the bubble break-up was observed when the inertial forces due to turbulent eddies were stronger than the forces due to surface tensions so that the bubble breakup rates were increased with the void fraction due to the reduced distances between bubbles [17]. As the detailed interfacing mechanisms and

their consequential impacts on the transition of flow regimes are closely related with the phase distribution, it has been treated as an important subject to resolve the flow mechanisms for establishing a phase distribution under gas–liquid two-phase flows. In this regard, the spectrum of the probability density function of bubble size [18], the tube diameter [19], the initial size and concentration distribution of bubbles [20,21] as well as the additional driving forces [22–25] can affect the phase distribution and the transition of flow patterns in the gas–liquid two phase flows. For modeling these two phase flows, the disclosure of the transport phenomena of the predominant two-phase parameters, namely the local void fraction and the interfacial area concentration, is essential. But very few theoretical foundations were established for relating these two-phase parameters to the measurable controlling parameters such as the interfacial velocities and bubble diameter. By assuming that the bubble breakup is occurred due to the collision of turbulent eddy with the bubbles; while the bubble coalescence takes place via random collisions induced by turbulence in a liquid phase, Ishii group [21] has derived and validated the transport equation for the interfacial area concentration under the steady fully developed flow condition.

With the presence of a spiky twisted tape in the gas–liquid two-phase tubular flow, the centrifugal forces and the flow separations tripped by the helically arranged spikes, which alter the local liquid turbulent structures and disturb the phase transition and void distribution, are expected to affect the interfacial structures, the transition of two-phase flow patterns and the heat transfer performances. Although no previous work investigated the two-phase flow phenomena in a tube fitted with the spiky twisted tape; but few relevant studies examined liquid–gas flows in a wire-coil inserted tube [22] and in the tubes where the centrifugal forces were induced by a twisted tape insert [23] or passing the flow through the helical coil [24]. Unlike the swirl tube in which the centrifugal forces prevail over the entire flow domain, the impacts of wire-coil insert on two-phase flows are triggered by the flow modifications in the near-wall region. With the wire-coil in the vertical air–water counter-current flow [22], the gas slug, which is longer than that in the likewise plain tube, rotates and is distorted in the radial direction. The wire-coil insert disturbs the liquid flow with the tendency to prevent wall-peak bubble distributions, which leads to the suppression of bubble coalescence in a wire-coil inserted tube. With high gas velocities, the liquid (water) is likely to trap in the spaces between neighboring coils near the tube wall that causes the lower void fraction in a wire-coil inserted tube than that in a plain tube. But with the presence of centrifugal force, the bubble region in a helical coil is reduced so that the bubbles have more chances to collision and coalescence [24]. Acting by the centrifugal forces on air and water with different densities, the bubbles are not freely suspended but are forced to accumulate by the secondary-flow convection that promotes the bubble coalescence and reduces the streamwise length for the transition from bubbly-to-plug flow [24]. With high gas velocities, the gas phase occupies the inner surface of the coil due to the radial pressure gradients generated by the centrifugal force. Liquid slugs convect along the outer wall of the helical coil with less obstructive effects caused by bubbles that behave like local stratified flows in the curvature direction.

With boiling heat transfer, the swirls induced by a twisted tape insert were more effective for increasing critical heat flux (CHF) than its HTE impacts so that the previous studies for nucleate boiling in a swirl tube with subcooled liquid were mostly aimed at CHF increase [23] with less attentions for HTE performances. In a two-phase swirl tube, the centrifugal forces are directed toward the tube wall and segregate liquid and gas phases with the liquid phase covering the heated wall to increase CHF. The point of nucleate boiling incipience shifted to the higher wall superheat, which could be increased by a factor of two with the heat transfer rates increased up to a factor three in post-dryout regimes [25]. This study investigates the impacts of fitting a spiky twisted tape into a vertical tube with bubbly air–water flow on heat transfer and pressure-drop performances by comparatively examining the two-phase flow structures, tube-averaged void fractions, pressure drops and local Nusselt numbers detected from the plain and swirl tubes. The two-phase flow patterns and bubble velocities in both plain and swirl tubes are measured visually using the high speed video camera. Experimental conditions are controlled by the air-to-water mass flow ratio (AW ratio) and Re_L for both plain and swirl tubes with the averaged void fractions, superficial gas/liquid velocities, local Nusselt numbers and pressure drops individually detected for each test tube. The range of AW ratios for each Re_L tested is initially determined from the flow visualization result that assures the bubbly air–water flow in the plain tube. The data set obtained with the air–water bubbly flows in the plain tube is treated as the reference results. The test conditions with the identical Re_L and AW ratios for the plain tube are repeated for the swirl tube with the spiky twisted tape insert. By way of controlling the Re_L and AW ratio at the prescribed test pressures, the similar range of bubble sizes at the air–water mixing plenum prior to the entry section of the plain or swirl tube is generated. With the same flow entry conditions in terms of bubble sizes, bubble distributions, Re_L and AW ratio, the differences in flow structures, pressure drop performances and heat transfer properties between the plain and swirl tubes are analyzed to highlight the impacts of the spiky twisted tape insert on the air–water bubbly tubular flow.

2. Experimental details

2.1. Test facility

Fig. 1a depicts the schematics of experimental test facility which consists of a air–water mixer (1), a 300 mm long developing section (2), a 420 mm long test section (3) and two quick-closing solenoid valves (4)(5) at the entry and exit of the test section for measuring the tube-averaged void fraction. The test section, developing section and air–water mixer are made from a transparent acrylic resin with the inner diameter of 20 mm for visual assess of the two-phase flow pattern. The acrylic test section (3) is replaced by heat transfer test module showed by Fig. 1b for measuring the heat transfer properties of air–water two-phase flows in the plain and swirl tubes. As the inner bore of the quick-closing valves (4) is 22 mm in diameter, the hydraulic boundary layers of each test tube will be tripped and re-developed at the entry edge of the test section. This arrangement allows for the examination of the thermal performances for developing flows which are expected to be different between the plain and swirl tubes with the single-phase and two-phase flows. Prior to entering the air–water mixer (1), the volume flow rate of water is adjusted and measured by the needle valve (6) and the digital volume flow meter (7) respectively. The dehumidified dry air is channeled into the air–water mixer, located in the bottom of the test apparatus, via four enter ports connecting with four cylindrical porous ceramics (8) through which the fine air bubbles with diameters between 0.5 and 1 mm are generated. As indicated in the air–water mixer, each porous ceramic rod is 7 mm long, 10 mm in diameter with the average pore diameter of 5 μm. The bubble size and flow regime are visualized from the snap shot of the Computerized Camera Digital (CCD) system (9) which is capable of taking 300 images in one second. This CCD system is also used to assist the allocation of the ceramic rods (8) in the air–water mixer in order to assure the basically uniform bubble distributions at the entrance of the test section. The

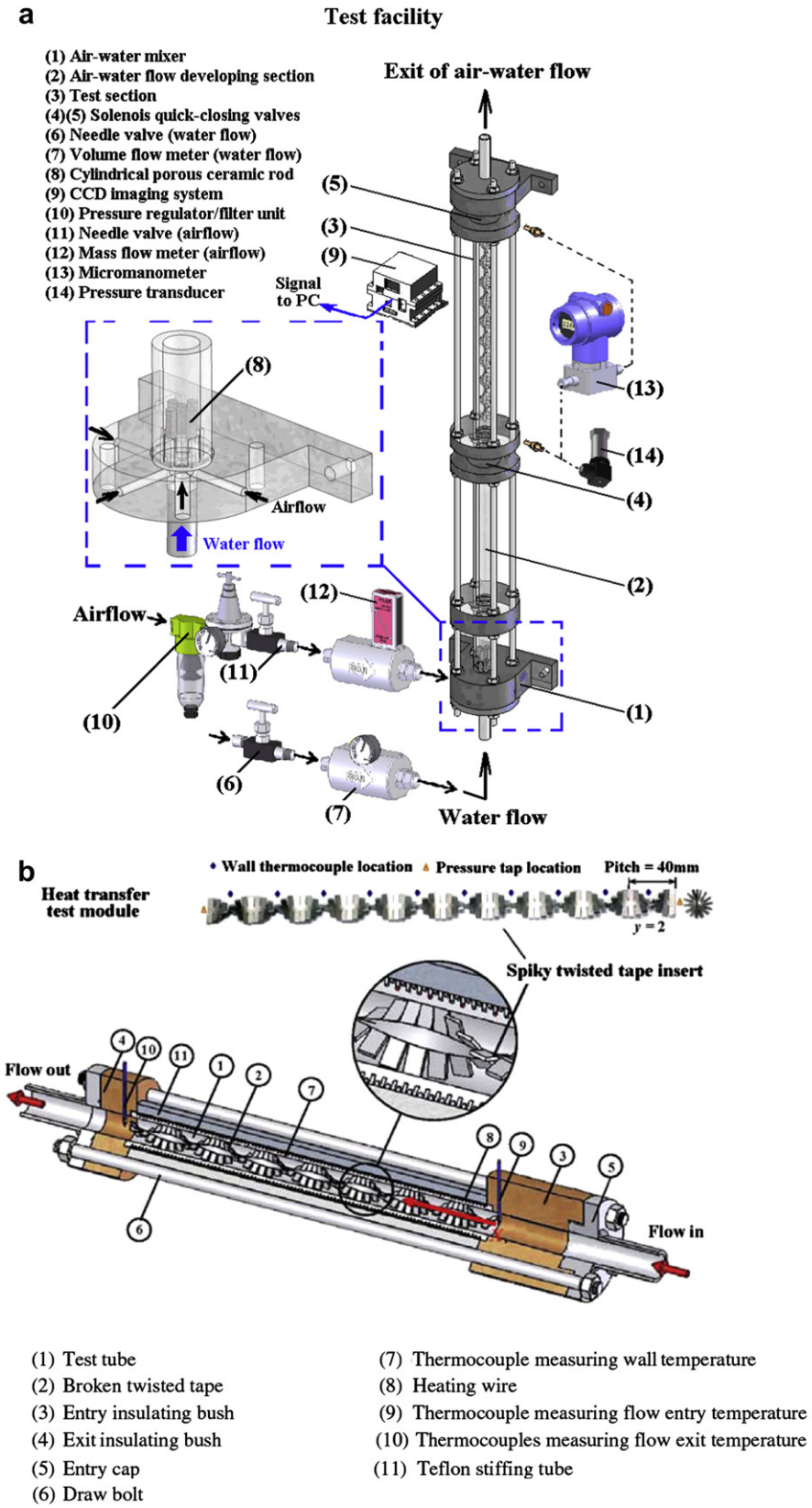

Fig. 1. (a) Test facility (b) heat transfer test module.

same range of bubble sizes leaving the air–water mixer is assured for all the tested two-phase flow conditions with plain and swirl tubes. For flow visualization tests, the camera was mounted on a tripod and aimed the angle normal to the test tube. The camera lens was fixed at a constant focal length resulting in the fixed viewing area. Although the flow images can be scanned on-line, all the images are post processed manually to measure the bubble diameter and/or the axial bubble velocities. The bubble diameter was estimated as the chord length through the bubble centroid parallel to the tube wall. About 20 measurements were taken for each image with the averaged value as the estimated bubble diameter. Prior to entering the air–water mixer, the airflow is channeled through a section consisting of pressure regulator and filtering unit (10), needle valve (11) and digital air mass flow meter (12) through which the airflow rate is adjusted and metered. Two solenoid quick valves (4)(5) are normally open and can close simultaneously when the electrical power is supplied. To avoid refraction image, the locations and strengths of four light sources are individually adjusted for each flow visualization test.

As indicated in Fig. 1a, two probing tubes are equipped with pressure taps of 0.5 mm diameter at the locations corresponding to the entrance and exit of the test section (3) to measure the pressure drops across the plain and swirl tubes. These pressure taps connect with a digital micromanometer (13) with the precision of 0.01 mm H_2O to detect the pressure drops across each test tube. However, with air–water two-phase flows, the spatial variations of interfacial pressures become temporal function resulting in the fluctuations in pressure drops across each test tube. The time averaged pressure drops over the entire test tube are calculated by averaging the measurements detected from the micromanometer over the scanning period about 15 s. At the flow entrance of the test section, a digital pressure transducer (14) was installed to detect the inlet pressure of air–water flow. Signals detected from the micromanometer (13) and the pressure transducer (14) were fed to the computer through the multi-channel Fluke data logger. For wall temperature measurements during each heat transfer test, the integrated average temperatures over a period of 3 seconds were performed with the time-averaged temperature data stored when the flow condition was satisfied. One K-type thermocouple probed into the entry core of the test tube to detect the flow entry temperature. At the exit of the test tube, five thermocouples with equal intervals were installed to detect the fluid exit temperatures which were averaged as the representative flow exit temperature for each test condition. Local fluid bulk temperatures were accordingly evaluated using the detected flow entry and exit temperatures by assuming the linear streamwise increase in each test tube heated by the basically uniform heat flux. The volume flow rate of airflow was determined based on the detected mass flow rate, flow entry pressure and temperature using ideal gas law. Having acquired the volume flow rates for air and water, the superficial gas and liquid velocities were accordingly defined. Measurements of pressure-drop, void fraction and flow visualizations for each test condition were separately performed under the isothermal conditions from the heat transfer tests. All the tests were performed at about the atmospheric pressures with Re_L and AW ratio selected as the controlling parameters for specifying the test conditions.

Fig. 1b depicts the heat transfer test module which has been previously reported in [15]. Only a brief description for the heat transfer test module is provided here. As depicted by Fig. 1b, the test tube (1), with or without the spiky twisted tape insert, was made from a seamless stainless steel tube with an inner diameter (D) of 20 mm, a wall thickness of 5 mm and a nominal length of 420 mm. The Teflon insulating bushes (3)(4), the entry cap (5) and the test tube (1) were tightened by four draw bolts (6) that gave the heating length of 420 mm. Coolant leakages from the contacts between the components constructing the test section were prevented by means of a series of internal O ring seals. A pair of twin start threads having the same pitch of 3 mm but different depths of 4 and 1.5 mm was machined on the outer surface of the test tube (1) to respectively install the wall thermocouples (7) and the Ni/Ch alloy resistance heating wire (8) for supplying the electrical heating power. Ten equally spaced K type wall thermocouples (7) were embedded in the deeper thread along the test tube. These wall thermocouples were controlled with a fixed radial distance of 1 mm away from the inner bore of the test tube at the axial locations corresponding to the mid-pitch locations for a spiky twisted tape with a twist ratio (y) of 2. As described previously, the fluid temperatures at the entry (9) and exit (10) were detected for the estimation of local fluid bulk temperatures. A Teflon stiffened tube (11) shielded the complete heat transfer test assemblies and added thermal insulation. However, in order to reduce the external heat loss, the outer surface of the stiffening tube (11) was wrapped with thermal insulation material. As indicated in Fig. 1b, the widths of this spiky twisted tape and each spike were 20 mm and 5 mm respectively. The straight spikes with a length of 7.5 mm joined the5 mm wide central twisted strip which formulated the spirally arranged spikes. There were 8 spikes over the axial span of a twist pitch with 180° rotation of the twisted tape. Relative to the flows in a tube with the continuous twisted tape insert, the swirls generated by the spiky twisted tape are weakened but the separated shear layers tripped by the spikes are induced, which further complicated the two-phase flow structures.

2.2. Program and data processing

The present experimental conditions were controlled by specifying Re_L and AW ratio under the test pressures at about 1–1.15 bars. For acquiring the liquid-phase turbulent conditions, Re_L at the entry of each test tube were controlled at 5000, 7500, 10,000, 12,500 and 15,000. Test range of AW ratio for each Re_L was selected to generate the bubbly air–water flows in the plain tube; which fell between 0.0004–0.01 and decreased with the increase of Re_L. Under these conditions, the superficial gas (U_{GS}) and liquid (U_{LS}) velocities were respectively in the ranges of 0.14–1.75 and 0.2–0.79 ms^{-1}. At each set of Re_L and AW ratios tested, the tube-averaged void fractions and pressured drops across the plain (ΔP_P) and swirl (ΔP_S) tubes were measured with the corresponding air–water flow images recorded under isothermal conditions. Heat transfer tests were subsequently performed to detect the local Nusselt numbers along the swirl (Nu_S) and plain (Nu_P) tubes at the identical test conditions for flow measurements. The hot spot wall temperatures were maintained at about 55 °C. The comparisons of heat transfer and flow measurements detected from the plain and swirl tubes reveal the impact of spiky twisted tape insert on the thermal fluid performances for the bubbly air–water tubular flows. Having acquired the heat transfer and pressure drop data for air–water flows in the plain and swirl tubes, the thermal performance index (η) defined as $(Nu_S/Nu_P)/(\Delta P_S/\Delta P_P)$ was accordingly evaluated to disclose the relative HTE gains under the increased pressure drop penalties due to the spiky twisted tape insert. A regression type analysis to derive the heat transfer correlations for the plain and swirl tubes using Re_L and AW ratio as the controlling variables was performed along the line of these research activities.

The local heat transfer property for this study was experimentally determined as $Nu_{S,P} = q_f D/[(T_w - T_b)k_f]$ where q_f, T_w, T_b and k_f are the convective heat flux, wall temperature at the inner core of each test tube, local fluid bulk temperature and the thermal conductivity of water evaluated at local T_b. For each test condition, the local convective heat flux was determined by subtracting the

external heat loss flux from the total heat flux supplied with axial wall conduction considered. The local heat loss fluxes were pre-calibrated as the function of wall-to-ambient temperature difference; while the estimation of axial wall conductive heat flux was based on the Fourier conduction law using the finite difference scheme for any set of axial wall temperature distributions measured. As the T_w distributions varied along each test tube to reflect the streamwise variations of local convective performances of the two-phase flow, the axial variations of heat loss flux and conduction heat flux were generated. Therefore the perfect uniformity of convective heat flux was impractical. With the adequate thermal insulation to reduce external heat loss from the test tube as depicted in Fig. 1b, the external heat loss for the present study was controlled to be less than 8.3% of the total heat flux supplied so that the basically uniform heat flux heating condition was simulated here. Estimations of experimental uncertainties for the present data reduction process were conducted [26]. The temperature measurements were the major sources for the uncertainties of *Nu*. With the heater power in the ranges of 2233–3148 W and the wall-to-fluid temperature differences between 25 and 42 K, the maximum uncertainties for *Nu* and Re_L were about 9.3% and 3.6% respectively.

3. Results and discussion

3.1. Two-phase flow structures

A set of instantaneous stereoscopic views of air–water two-phase flows which compare the flow patterns in the plain and swirl tubes at five tested Re_L with two AW ratios of 0.0006 and 0.002 is collected in Fig. 3. The different two-phase flow structures between the plain and swirl tubes are readily visible by examining each comparative group depicted in Fig. 2. The range of AW ratios at each predefined Re_L for the present test program is controlled to generate the dispersed bubbly flows in the plain tube where the relatively small bubbles compared with the tube diameter randomly rise over the test tube as typified by all the plain-tube images in Fig. 2. For such dispersed bubbly flow in the plain tube, the gas phase is dispersed into small spherical like bubbles with diameters around 0.6–2.6 mm by the turbulent eddies. The formation of finely dispersed bubbly flow in the plain tube is clearly visible in Fig. 2c–e. With Re_L reaching turbulent levels in the range of 5000–15,000, the process of bubble break-up along the plain tube due to the turbulent forces in the liquid phase that overcome the gas–liquid interfacial tension results in the continuous reduction of bubble diameters when Re_L increases at each AW ratio tested. Increase of AW ratio at each tested Re_L increases the mass flux of gas phase. This accordingly increases the averaged void fraction (α) and the flux of bubble number density in both plain and swirl tubes. Due to the increased α and bubble number density by increasing AW ratio for the plain tube air–water flow, the bubble diameters are decreased and the interfacial area concentration is increased as AW ratio increases for each Re_L. This is also demonstrated in Fig. 2 by comparing the images collected at two AW ratios for each Re_L. Although the flow regimes under all the test conditions remain as dispersed bubbly flows in the plain tube, the impacts of AW ratio and Re_L on phase distributions, interfacial area concentrations and liquid-phase turbulent activities can cause profound influences on both heat-transfer and pressure-drop performances which will be later examined.

In the present swirl-tube, the centrifugal forces induced by the twisted tape along with the separated shear layers tripped by the spiral spikes generate local variations in pressure gradients, alter the liquid-phase turbulent structures and induce the swirling air–water two-phase flows. The consequential impacts of these flow phenomena triggered by the spiky twisted-tape modify the phase distributions in the swirl tube from the plain-tube conditions by changing the processes of bubble coalescence and disintegration as seen in Fig. 2. In the swirl tube, the centrifugal forces introduce the radial segregating effect by driving the higher density liquid-phase fluid toward the tube wall with the inner core occupied by the low density gas-phase fluid. Due to the segregating effects induced by the centrifugal forces, the air bubbles in the swirl tube are concentrated in the tube core and drifted with the swirls as typified by the instantaneous flow images shown in Fig. 2. Such bubble concentration in the core region of the swirl tube enhances bubble collisions and therefore bubble coalescences with the radial α distribution to be the core-peaking profile. As the transition to slug flow was always preceded by a core peaking void-fraction profile, the centrifugal force induced by the twisted-tape insert deems to advance the flow transition from the dispersed bubbly flow to the slug flow. It is also noticed that, with small AW ratio and high Re_L for the swirl tube, the superficial velocities of the gas phase that biases to the tube core are slower than the liquid-phase superficial velocities as the liquid flow in the swirl tube is allowed to flow along the tube wall with less obstacles from the freely dispersed bubbles in the likewise plain tube. The bubble can have negative slip velocity against liquid phase at low AW ratios due to the biased (core-peaking) gas-phase distributions in the present swirl tube, which phenomenon has also been observed for the air–water two-phase flow in the helical coil where the centrifugal forces are induced by the curvature of the flow passage [24]. Nevertheless, for the flow conditions examined here, the two-phase flow structures in the swirl tube are not yet evolved into the slug flows as the bubble plenums that swirl along the tube core are rather continuous than the periodical and intermittent large gas plugs in slug flows. While the dispersed bubbly flow is developed in the plain tube, the continuous large eddies including bubble clusters that fill up the tube core in the swirl tube characterize the agitated two-phase bubbly flows in the swirl tube. The successive images taken from the swirl tube also reveal that the moving directions of these bubble clusters are random due to the large scale liquid-phase eddy motions. As indicated by Fig. 2f, the bubble coalescence, bubble break-up and, in particular, the bubble reversion due to local turbulent eddies are frequently observed in the swirl tube during and after these bubbles squeezing through the gapes between two neighboring twisted spikes. Under conditions of high Re_L and AW ratios in the swirl tube as typified by Fig. 2d and e with AW = 0.002, the higher degrees of bubble coalescences result in the coherent distorted large bubbles that roll and rise along each spiral pathway with many dispersed small bubbles in the liquid films between the coherent large bubbles and the tube wall. By comparing the swirl-tube flow images with AW = 0.0006 and 0.002 at Re_L = 12,500 and 15,000 as seen in Fig. 2d and e, the impact of AW ratio on flow structures in the swirl tube is revealed. At AW = 0.0006, Fig. 2d and e depicts the continuous spiral bubble clusters at the tube core of the swirl tube. With AW = 0.002, the coherent large rolling bubbles with dispersed tiny bubbles in the near-wall liquid film characterize the two-phase swirl-tube flow pattern. With the presence of the coherent and rolling large bubbles in the swirl tube at high Re_L and AW ratio, the boundaries and shapes of the water–air interfaces are constantly changed leading to unstable interfacial structures. For such flow scenarios observed in the swirl tube with high Re_L and high AW ratios, a wider spectrum of bubble size is expected to affect the transition of phase distribution and lead to the earlier transition from the bubbly flow to churn slug/forth flow in the swirl tube. Nevertheless, the air–water two-phase flow images compared in Fig. 2 between plain and swirl tubes have demonstrated the considerable modifications in interfacial structures, phase distributions and transitions of flow structures by way of inserting the spiky twisted tape.

As an important parameter for theoretical treatments of the interfacial transports of two-phase flows, the void fractions

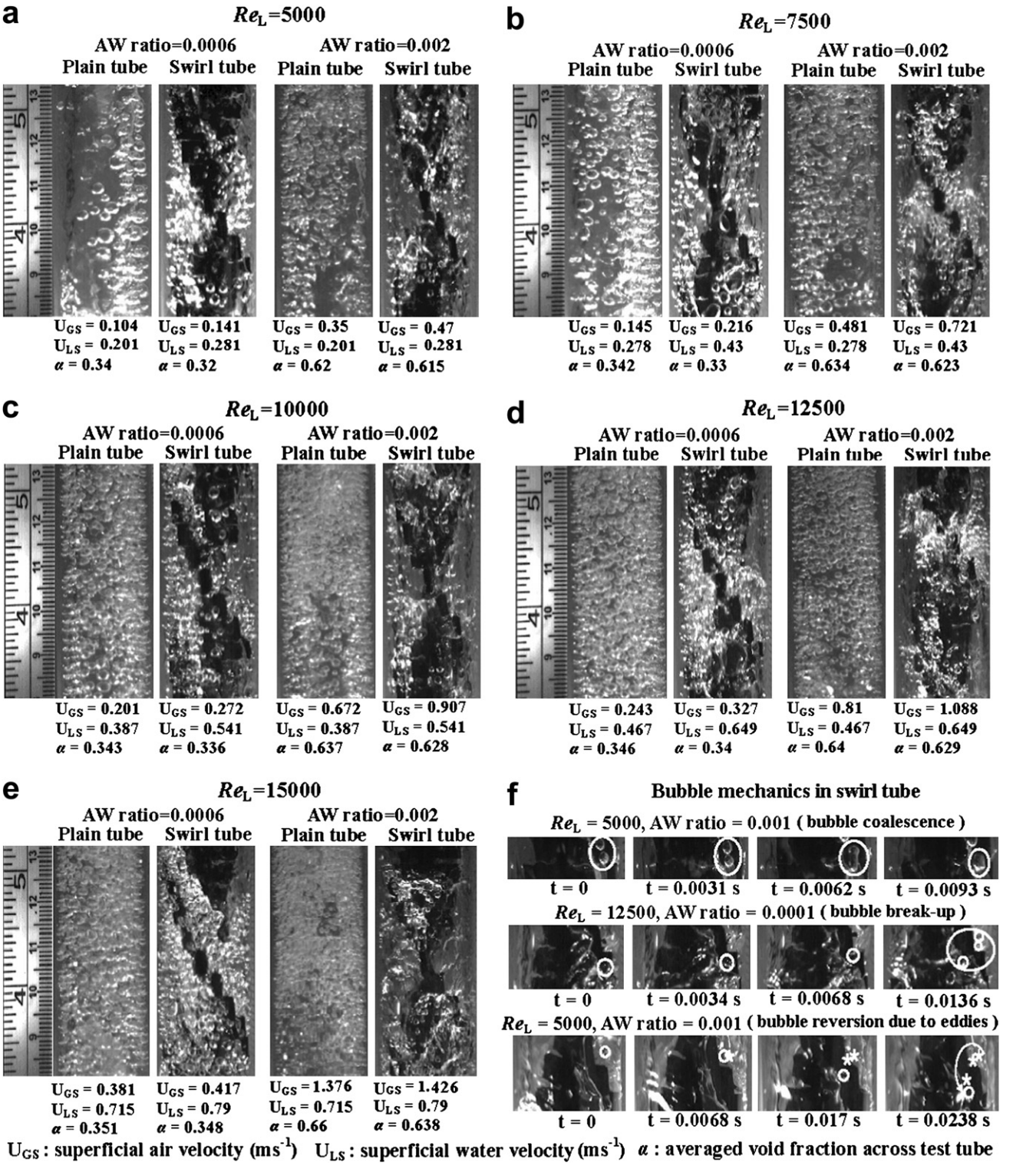

Fig. 2. High-speed air–water two-phase flow images at AW = 0.0006 and 0.002 with Re_L = 5000, 7500, 10,000, 12,500, 15,000.

detected from the present plain and swirl tubes are examined with the attempt to identify the α correlation. Fig. 3a compares the variations of void fraction (α) against gas-phase superficial velocity (U_{GS}) at each tested Re_L for both plain and swirl tubes. Following the typical trend of α variation against U_{GS} for a two-phase bubbly flow, the averaged void fractions in the tested plain and swirl tubes as seen in Fig. 3a for each Re_L increase with the increase of U_{GS}. But the void fractions in the swirl tube are constantly lower than the plain-tube counterparts. The lower void fractions in the present swirl tubes indicate the thicker water films over the tube wall with certain amount of water trapped in the twisted gaps between neighboring spikes through the entire spiky twisted tape. In this respect, the thickened water films as well as the trapped liquid in the spiky twisted tape that

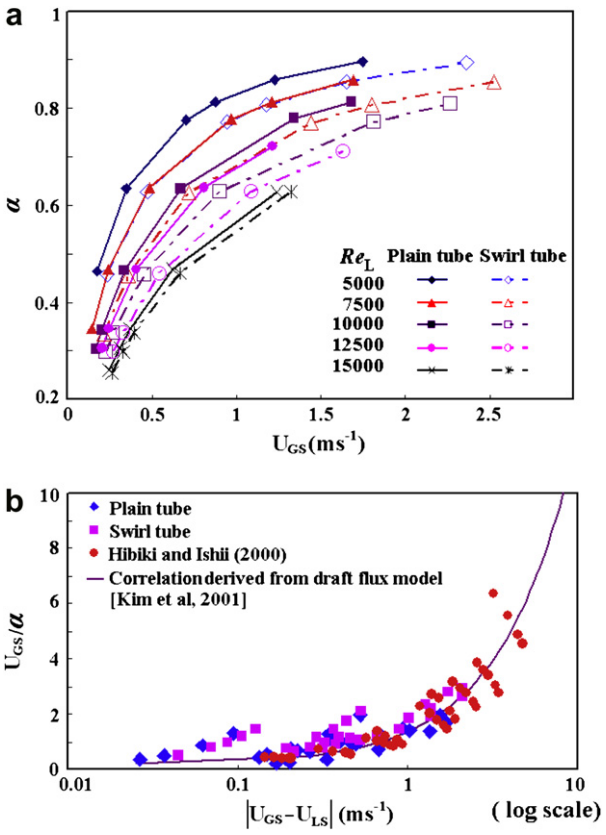

Fig. 3. (a) Variations of void fraction against superficial gas-phase velocity. (b) Normalized void fraction against gas-to-liquid slip velocity.

is in contact with the heated tube wall are in favor of CHF elevations.

As well as for the validation, the experimental α data collected from the present plain and swirl tubes are also compared with the local α measurements reported by Hibiki and Ishii [27] for air–water bubbly flows in vertical plain tube. These experimental void fractions are attempted to be correlated using the drift flux model with the gas drift flux corresponding to Taylor bubble rising velocity in a stationary liquid, which has been previously proposed by Kim et al. [22] to correlate their α measurements for the counter-current air–water flow in a vertical tube with wire-coil inserts. To comply with this drift flux model, the void fraction is converted into U_{GS}/α and plotted against the absolute slip velocity $|U_{GS} - U_{LS}|$ between the superficial gas and liquid velocities. As seen in Fig. 3b, the present measurements of U_{GS}/α for the plain tube agree favorably with the experimental data reported by Hibiki and Ishii [27]. It is also noticed that the data clusters collected from the present swirl tube converge into the same data trend with those detected from the plain tubes. These converged U_{GS}/α versus $|U_{GS} - U_{LS}|$ data-trends for both plain and swirl tubes observed in Fig. 3b also agree well with the correlation derived from the drift flux model [22], which expresses the void fraction as

$$\alpha = U_{GS}/(V_{Gj} + C \times |U_{GS} - U_{LS}|) \quad (1)$$

In equation (1), C is the two-phase distribution parameter for a circular tube defined as $1.2 - 0.2\sqrt{\rho_G/\rho_L}$; V_{Gj} is the gas drift flux evaluated as $0.35\sqrt{g(\rho_L - \rho_G)D/\rho_L}$. As equation (1) reasonably correlate the various void fractions detected from the present plain and swirl tubes, the round tube [27] and the air–water flow in a vertical tube with wire-coil inserts [22], the applicability of equation (1) for void fraction of two-phase bubbly flows in tubes is reconfirmed.

3.2. Pressure drop measurements

The pressure drop measurements for the single phase water flow in the plain and swirl tubes at AW = 0 were detected as the reference datum against which the ΔP measurements collected from the air–water flows were compared in order to assess the influences of AW ratio on ΔP. As well as for validations, the ΔP values converted from the Blasius equation for plain tube and from our previous pressure-drop correlation for the swirl tube [15] with single-phase flow conditions (AW = 0) are respectively compared with the present ΔP measurements with air–water flows in Fig. 4a and b. With the presence of air bubbles in both plain and swirl tubes, the pressure drops across the test tube increase dramatically from the AW = 0 conditions as seen in Fig. 4a and b. The additional frictional, accelerational and form drags prevailing over the interfacial areas due to the water-to-air interfacial activities of these rising bubbles, which mainly depend on the shape and size of each bubble, have considerably elevate the pressure drops across the plain and swirl tubes. As the variation of AW ratio at each Re_L simultaneously alter the sizes (pressure drag) and the interfacial areas (frictional drag) of the air bubbles, the AW impacts on pressure drops across each test tube become the competitive results between the increased (decreased) friction and pressure drags via the AW impacts on the interfacial structures. Using the plain-tube results for illustrations, the averaged bubble sizes for the flow images depicted in Fig. 2a at $Re_L = 5000$ with AW = 0.0006 and 0.002 are about 2.8 and 2.3 mm; while the averaged bubble sizes with $Re_L = 15{,}000$ with AW = 0.0006 and 0.002 are about 1.75 and 1.5 mm. The present bubbly two-phase flows with relatively large bubbles at low Re_L ($5000 \le Re_L \le 7500$) indicates the pressure-drag

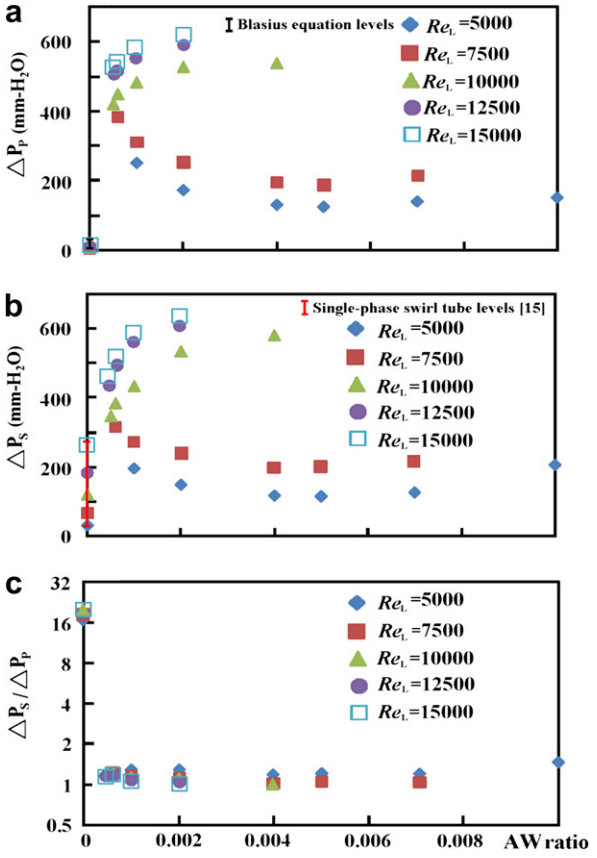

Fig. 4. Variations of (a) ΔP_P (b) ΔP_S (c) $\Delta P_S/\Delta P_P$ against AW ratio at $Re_L = 5000$, 7500, 10,000, 12,500 and 15,000.

dominant scenarios in Fig. 4a and b. As AW increases at $Re_L = 5000$ and 7500, the averaged bubble diameters are consistently deceased with the attendant reductions in the pressure drags due to the decreased bubble-sizes; although the increased friction drags due to the increased interfacial areas take place simultaneously. However, as depicted in Fig. 4a and b with $Re_L = 5000$ and 7500, the increase of AW from 0.005 onward incurs the ΔP recoveries; which implies the transition from pressure-drag to friction-drag dominant conditions for the interfacial pressure drops required to keep up the upward air–water bubbly flows. With $Re_L = 10{,}000$, 12,500 and 15,000, the interfacial friction drags play the dominant role in determining the overall pressure drop across the test tube so that the increase of AW ratio keeps increasing ΔP by way of increasing the interfacial friction drags although the pressure drags for individual bubbles can be reduced as a result of the reduced bubble size. Nevertheless, at each fixed AW ratio, the data trends collected in Fig. 4a and b suggest the consistent increase of ΔP as Re_L increases due to the increased U_{GS} and U_{LS}.

The increased pressure-drop penalty due to the spiky twisted tape insert is indexed by the ratio between the pressure drops across the swirl (ΔP_S) and plain (ΔP_P) tubes at the same Re_L and AW ratio. Variations of $\Delta P_S/\Delta P_P$ against AW ratio at all Re_L tested are depicted in Fig. 4c. With single-phase flows (AW = 0), the $\Delta P_S/\Delta P_P$ ratios are raised to 18–22 so that the wall drags added by the spiky twisted tape for the single-phase tubular flow play the dominant role in pressure-drop augmentations. With the air–water bubbly flows, the $\Delta P_S/\Delta P_P$ ratios fall dramatically to the range about 1.2–1.6 in Fig. 4c; while the pressure drops in both test tubes with air–water bubbly flows are considerably elevated from the AW = 0 conditions as depicted in Fig. 4a and b. The considerable reductions in $\Delta P_S/\Delta P_P$ ratios for air–water bubbly flows from the AW = 0 conditions suggest that the drags induced by the air–water interfacial structures are predominant rather than the wall drags added by the spiky twisted tape insert. This result has been previously reported in [28] that the pressure drops for upward gas–liquid two-phase flows were mainly an indication of liquid holdup and were weekly dependent on wall drags. The 20–60% increases of pressure drops across the swirl tube with air–water flows are mainly caused by the different interfacial structures between the swirl and plain tubes. As revealed by Fig. 2, the centrifugal forces induced by the spiky twisted tape have led to a pair of coherent bubble streams that swirls in the helicoidally twisted passages. Similar to the slug flows which required the large pressure gradients between the front and the rear of the liquid slug to be pushed against the friction drags among the air–water interfacial structures [24], the swirling coherent bubble streams developed in the present swirl tube require the higher pressure gradients to attain the same Re_L. As a result, the $\Delta P_S/\Delta P_P$ ratios in Fig. 4c are all above than unity.

3.3. Heat transfer measurements and correlations

Heat transfer measurements detected by this study are quantified as Nu_P and Nu_S for the plain and swirl tubes respectively so that the heat transfer correlations can be expressed as functions of dimensionless parameters, namely Re_L and AW ratio, and the $Nu_{P,S}$ at AW = 0 conditions can be readily compared with Dittus–Boelter correlation [29] and our previous results derived from the likewise swirl tube with single-phase airflow [15] for validations. Fig. 5a,b and c,d respectively depict the axial heat transfer variations along the plain and swirl tubes with single-phase water flow (AW = 0). In the plain tube, the axial Nusselt number distribution for each Re_L tested follows the typical boundary-layer flow pattern that decays exponentially toward the fully developed level after the water flow travels about 5 tube diameters as seen in Fig. 5a. The higher Nu_P values in the developing flow region are mainly attributed to the

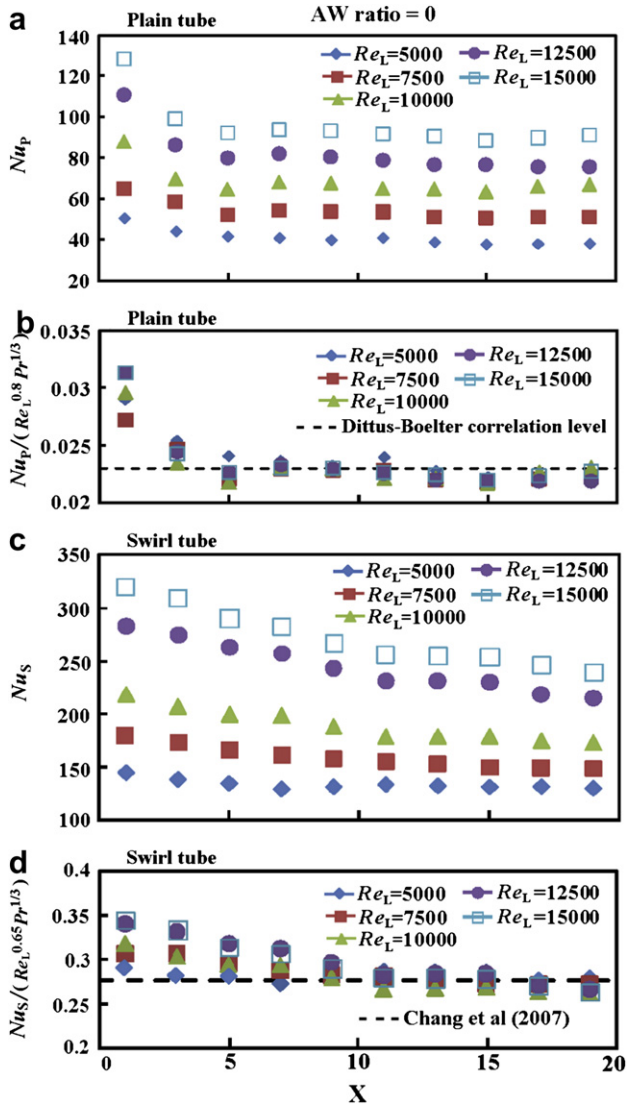

Fig. 5. Axial variations of (a) Nu_P (b) $Nu_P/(Re_L^{0.8}Pr^{1/3})$ (c) Nu_S (d) $Nu_S/(Re_L^{0.65}Pr^{1/3})$ at AW = 0 with Re_L = 5000, 7500, 10,000, 12,500 and 15,000.

developing boundary layers. At each X location, Nu_P increases as Re_L increases. With AW = 0, the normalized heat transfer levels in terms of $Nu_P/(Re_L^{0.8}Pr^{1/3})$ with $5000 \le Re_L \le 15{,}000$ collapse into a tight data band in the developed flow region as shown in Fig. 5b. The converged $Nu_P/(Re_L^{0.8}Pr^{1/3})$ value in the developed flow region for the plain tube agrees favorably with the Dittus–Boelter correlation as compared in Fig. 5b. With swirl tube at AW = 0, the axial Nu_S distribution obtained at each Re_L as seen in Fig. 5c still follows the exponential decay toward a fully developed Nu_S level. But the developing length is extended from the plain-tube condition to about 10 tube diameters due to the longer settling length required for the development of swirls. By normalizing the present Nu_S data with $Re_L^{0.65}Pr^{1/3}$, all the heat transfer measurements in the developed flow region collapse into a tight data band that agrees well with our previous correlations derived from the air-flow in the likewise swirl tube [15]. The agreements between the $Nu_S/(Re_L^{0.65}Pr^{1/3})$ data collected from the single-phase water flow and airflow [15] suggest that the Pr impacts for the present swirl tube with single-phase flow are well taken into account by $Pr^{1/3}$ in the Nu_S correlation. The cross-examination of the numerical Nu_P and Nu_S data indicates that the Nu_S/Nu_P ratio at AW = 0 fall in the range

of 2.75–3.25. As reported previously [15], the spiky twisted tape insert in the tube induces a pair of swirling flows and trips numerous separated shear layers downstream these spirally arranged spikes, which interact together to promote the fluid mixing and turbulence intensities and cause the attendant increases in heat-transfer levels and pressure drops across the swirl tube.

With air–water bubbly flows, the dispersed bubbles in plain tube and the swirling coherent bubble-streams that concentrate at the core region of swirl tube distinguish two different interfacial flow structures as demonstrated by Fig. 2. Impacts of these interfacial flow structures on wall-to-fluids heat transfer properties at each tested Re_L are revealed by comparing the axial Nu_P and Nu_S distributions obtained with the single-phase (AW = 0) and two-phase flow conditions in Fig. 6. With the agitated air-bubbles to augment the mass/heat flux exchanges among the air–water interfacial structures; while the water film is constantly covered over the inner wall for the bubbly flow regime, heat transfer levels along both plain and swirl tubes increase dramatically from the AW = 0 condition. This is clearly shown by each plot of Fig. 6 in which the local Nu_P and Nu_S increase consistently as AW increases for each Re_L tested. Ranges of such AW-driven upward Nu_P and Nu_S spreads are increased as Re_L increases, indicating the interdependent Re_L and AW effects on Nu_P and Nu_S. Although the AW-driven HTE impacts on the overall wall-to-fluids heat transfer performances follow the similar qualitatively trend for both plain and swirl tubes, the subtle differences for HTE mechanisms lie in the different interfacial bubbly air–water structures between the plain and swirl tubes. As revealed in Fig. 2 for the plain tube, the increased AW ratio (Re_L) at a fixed Re_L (AW ratio) increases the bubble density flux by reducing the bubble size in the dispersed bubbly flow. Although the large-scale secondary flows in the plain tube are absent, the small and unstable eddies are induced by the dispersed and wafting air bubbles which promote local exchanges of momentum and heat fluxes. When the density flux of these randomly rising dispersed bubbles is increased, the local fluid mixings due to the small and fluctuating turbulent eddies are amplified with more frequent agitations on the liquid-phase boundary layers over the plain-tube wall. The augmentation of these localized small-scale eddies, triggered by the increase of AW ratio (Re_L) at a fixed Re_L (AW ratio), leads to the enhanced HTE impacts for the plain tube with bubbly flows. However, the centrifugal forces in each helically twisted passage of the swirl tube tend to segregate the liquid and gas phases; and consequently induce the coherent bubble-streams that concentrate at the tube core and spiral about the tube central axis. With such particular interfacial flow structure in the swirl tube, the increased averaged void fraction across the swirl tube as a result of increasing AW ratio (Re_L) at a fixed Re_L (AW ratio) cause the acceleration of water film that covers the tube inner wall. Accompanying with the promoted turbulent activities in the swirls, the accelerated and agitated water film augments the HTE impacts further for the swirl tube by way of increasing AW ratio (Re_L) at a fixed Re_L (AW ratio). These different flow mechanics triggered by varying the AW ratio (Re_L) between the plain and swirl tubes for HTE impacts can lead to different interdependent AW and Re_L effects on Nu_P and Nu_S correlations, which will be later demonstrated. Nevertheless, justified by the axial Nu_P decay as shown in Fig. 6, the axial developing length in the plain (swirl) tube with air–water two-phase flow is clearly extended from 5 (10) to about 15 tube diameters. This is interesting to note in Fig. 6 that the developing length for the swirl tube with air–water two-phase flow is also about 15 tube diameters. In addition to the boundary layer development, the streamwise development of air–water interfacial structures tends to play the predominant role in determining the axial Nu_P and Nu_S distributions. Relative to the axial heat transfer variations at AW = 0 conditions as compared in each plot of Fig. 6, the typical exponential Nu_P or Nu_S decay for a tubular single-phase flow is somewhat yielded by the interfacial two-phase structures. In this respect, the relative Nu_P (Nu_S) elevations near the flow entrance for the present two-phase flow conditions are less effective from the AW = 0 scenarios. Therefore the streamwise developments of near-wall fluid temperature gradients in the radial direction are modified by these rising bubbles through their agitating effects on the boundary-layer development.

Local Nu_P and Nu_S measurements detected from the developed flow region in the plain and swirl tubes at each AW ratio and Re_L tested are averaged as $\overline{Nu}_P$ and $\overline{Nu}_S$ for devising the heat transfer correlations. In quest of the controlling dimensionless parameters in $\overline{Nu}_{P,S}$ correlations, the aforementioned heat transfer results have demonstrated that Re_L and AW ratio can serve as the controlling variables as long as the bubbly flow regime is pre-defined. Particularly, as Re_L and AW ratio can be directly assessed as the predetermined design conditions or by the direct measurements, the selection of Re_L and AW ratio as the determining variables for $\overline{Nu}_{P,S}$ can offer great conveniences for engineering applications. Based on the flow visualization results to control all the flow conditions in the bubbly flow regime, which is re-confirmed by the α correlation derived from the drift flux model [22] as depicted by Fig. 3, $\overline{Nu}_{P,S}$ correlations are derived as functions of AW ratio and Re_L. Fig. 7 depicts the variations of (a) $\overline{Nu}_P$ and (b) $\overline{Nu}_S$ against Re_L at each AW ratio tested. As seen in Fig. 7, each AW-ratio controlled data trend shows the consistent $\overline{Nu}_{P,S}$ increase as Re_L increases. At each tested Re_L, $\overline{Nu}_{P,S}$ also increases with the increase of AW ratio for the plain and swirl tubes. Justified by all the Re_L driven data trends displayed in Fig. 7 and the inter-correlative impacts of Re_L and AW ratio on wall-to-fluid heat transfer rates, $\overline{Nu}_{P,S}$ are derived as $A\{AW\}\times Re_L^{B\{AW\}}$ where the A coefficient and B exponent are functions of AW ratio. Fig. 8 compares the varying manners of (a) A-coefficient (b) B-exponent against AW ratio between the plain and swirl tubes. In view of experimental studies, it is worth noting that the B exponent in Nu correlations often decreases from 0.8 (smooth-walled duct level) to about 0.5–0.65 for the channels with ribs, dimples or twisted-tape insert by way of inducing local and/or large-scale secondary flows that modify the near-wall momentum/heat exchanges from the smooth-walled conditions. Differential B exponents in Nu correlations reflect different near-wall flow structures. As seen in Fig. 8, the varying trends of A, B values against AW ratio are different between the plain and swirl tubes due to the different interfacial air–water structures in the plain and swirl tubes as typified in Fig. 2. For the swirl tube in which the gas-to-liquid segregation develops as a result of the centrifugal forces, the stronger bubble coalescence is observed in Fig. 2 at AW = 0.002 from the AW = 0.0006 conditions. With the higher AW ratio for swirl tube, the water film covering the inner tube-wall tends to be stratified from the coalesced air bubbles which occupy the tube core. The near-wall flows in the swirl tube tend to recover into the turbulent boundary-layer flows with less degree of bubbly disturbances as AW ratio increases. Therefore, as showed by Fig. 8, the B exponents for the swirl tube are increased from 0.65 [15] at the AW = 0 condition toward 0.8 as AW ratio increases. Such increase in B exponents for the swirl tube incurs the corresponding decrease in A-coefficient as AW ratio increases. Nevertheless, when the two-phase flow patterns transits to slug or annual flows from the present bubbly flows, the B exponent is subject to variations from the boundary layer type behavior. But with the plain tube, the increase of AW ratio tends to enhance the local small eddies as well as the bubbly disturbances on the water film that covers the tube wall as seen in Fig. 2. Such impacts caused by increasing AW ratio affect the near-wall flow structures in the plain tube with the

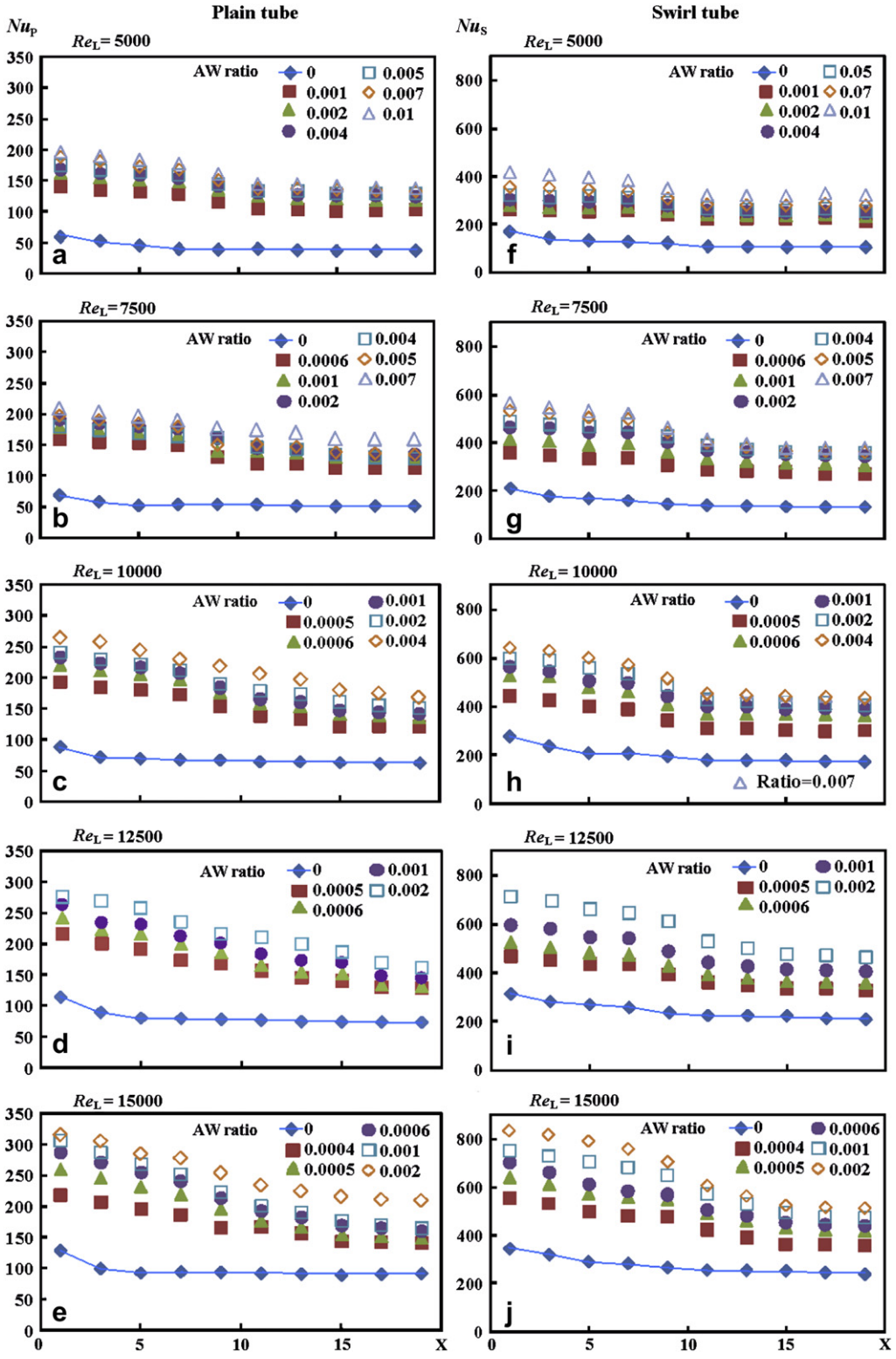

Fig. 6. Comparison of axial Nu_P and Nu_S distributions with various AW ratios at $Re_L = 5000$, 7500, 10,000, 12,500, 15,000.

tendency to deviate from the turbulent boundary layers to the agitated wall-layers stirred by the small eddies. These localized temporal eddies, which are induced by the dispersed rising bubbles, are intensified due to the increased bubble density flux at the higher AW ratios. In this respect, the previous study for tubular bubbly boiling flow has identified the vapor bubble sliding as the manifesting HTE mechanism to augment the wall-to-fluid heat transfer properties as evidenced by their higher heat transfer coefficients for upflow than for downflow under otherwise identical test conditions [30]. With the dominant HTE mechanism shifting from the typical boundary layer turbulent flow, the B exponent for the plain tube as depicted in Fig. 8b is consequently

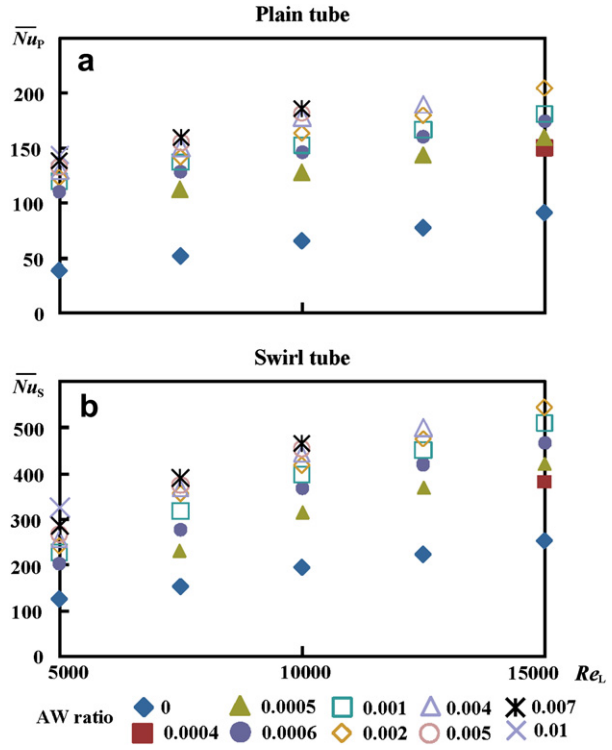

Fig. 7. Variations of (a) $\overline{Nu}_P$ (b) $\overline{Nu}_S$ against Re_L at various AW ratios.

reduced by increasing AW ratio; while the corresponding increase in *A*-coefficient is observed in Fig. 8a. With AW = 0 conditions for single phase water flows, the data trends revealed in Fig. 8a and b respectively recover the Dittus–Boelter correlation [29] for the plain tube and our previous correlation derived for single-phase flow in the likewise swirl tube [15]. It is also worth noting that the $\overline{Nu}_{P,S}$ measurements at the fixed AW ratios of 0.0004 and 0.01 are limited to $Re_L = 15{,}000$ and 5000 in order to maintain the bubbly flows in the plain tube. Therefore, the *A*, *B* values indicated in Fig. 8a and b at the flow conditions of AW = 0.0004 ($Re_L = 15{,}000$) and AW = 0.01 ($Re_L = 5000$) are extrapolated from the AW-controlled *A*, *B* trends depicted in Fig. 8a and b. The experimentally detected $\overline{Nu}_{P,S}$ at the conditions of AW = 0.0004 ($Re_L = 15{,}000$) and AW = 0.01 ($Re_L = 5000$) are used to validate the extrapolated *A*, *B* values at these two set of flow conditions. As depicted by Fig. 8a and b, the varying trends of *A* coefficient and *B* exponent, which are collected from the correlations of $\overline{Nu}_{P,S} = A\{AW\} \times Re_L^{B\{AW\}}$ using the results displayed in Fig. 7, show the asymptotic trends that comply well with the exponential functions. Having determined the *A* coefficient and *B* exponent as the exponential functions of AW ratio from the data trends revealed in Fig. 8, the correlations for $\overline{Nu}_P$ and $\overline{Nu}_S$ are respectively derived as equations (2) and (3).

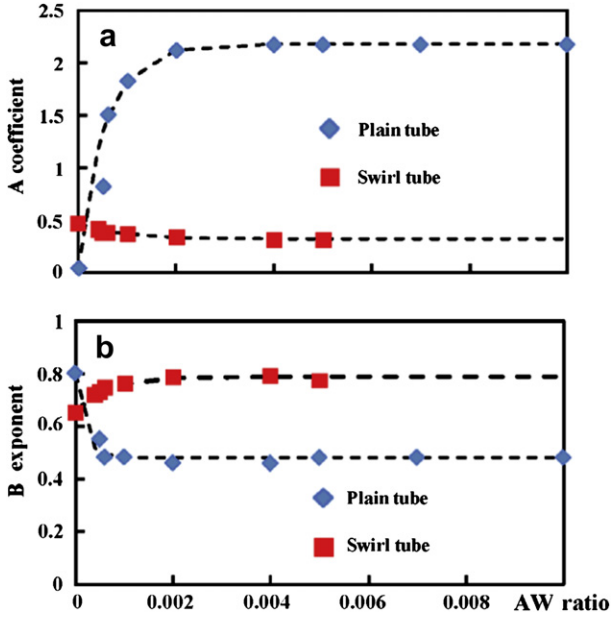

Fig. 8. Variations of (a) *A* coefficient (b) *B* exponents in $\overline{Nu}_P$ and $\overline{Nu}_S$ correlations against AW ratio.

$$\overline{Nu}_P = \left(2.17 - 2.132 \times e^{-1820\times AW}\right) \times Re^{0.479+0.321\times e^{-5160\times AW}} \quad (2)$$

$$\overline{Nu}_S = \left(0.323 + 0.1366 \times e^{-1164\times AW}\right) \times Re^{0.79-0.135\times e^{-1074\times AW}} \quad (3)$$

Equations (2) and (3) respectively permit the evaluation of the interdependent and individual Re_L and AW-ratio effects on $\overline{Nu}_P$ and $\overline{Nu}_S$ for the tubular air–water bubbly flows without and with the spiky twisted tape insert. Equations (2) and (3) agree with the single phase water flow condition at AW = 0 as described by the Dittus–Boelter correlation [29] and our previous work derived for the present swirl tube [15] respectively. However, as the Prandtl number effect is not examined here, equations (2) and (3) can not recover the single phase air flow condition with AW → ∞. The overall accuracies of $\overline{Nu}_{P,S}$ correlations are examined by comparing the calculated and experimental $\overline{Nu}_{P,S}$ as depicted in Fig. 9. The maximum discrepancy of ±20% between the experimental and correlation results is achieved for 96% of the entire $\overline{Nu}_{P,S}$ data. Also clearly shown in Fig. 9 is the higher $\overline{Nu}_S$ over the $\overline{Nu}_P$ cluster, indicating the heat transfer improvements offered by the spiky twisted tape insert for the tubular air–water bubbly flows. The HTE impacts generated by the spiky twisted tape insert are subsequently analyzed by examining the ratio between $\overline{Nu}_S$ and $\overline{Nu}_P$ which are detected at the same Re_L and AW ratio from the plain and swirl tubes.

Fig. 10 depicts the variations of $\overline{Nu}_S/\overline{Nu}_P$ against AW ratio at each Re_L tested. For the single-phase flow (AW = 0) conditions, $\overline{Nu}_S/\overline{Nu}_P$ consistently drops between the range of 2.75 and 3.25 as Re_L increases. As *B* exponents in $\overline{Nu}_S$ and $\overline{Nu}_P$ correlations at AW = 0 are respectively 0.65 and 0.8, $\overline{Nu}_S/\overline{Nu}_P$ systematically decreases as Re_L increases; which indicates the weakened HTE impacts at the high Reynolds numbers for single phase flows. The Re_L and AW impacts on the HTE performances attributed from the spiky twisted-tape

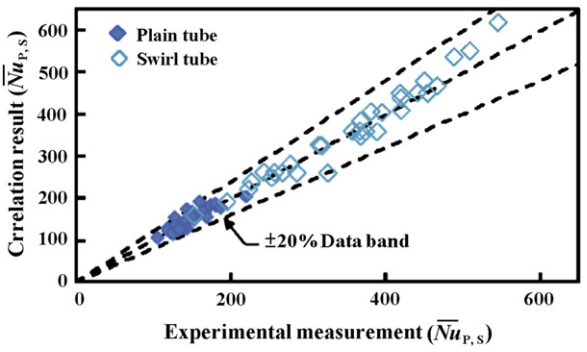

Fig. 9. Comparisons of correlated $\overline{Nu}_P$ and $\overline{Nu}_S$ results with experimental measurements for plain and swirl tubes.

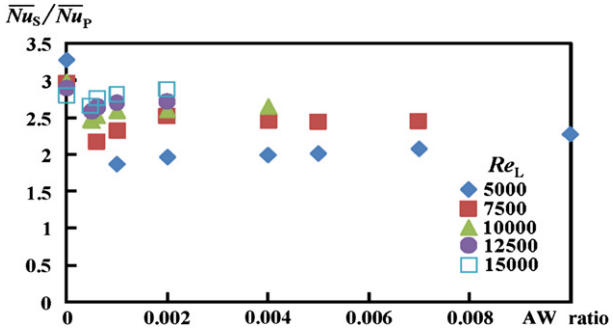

Fig. 10. Variations of $\overline{Nu}_P/\overline{Nu}_S$ against AW ratio at $Re_L = 5000$, 7500, 10,000, 12,500, 15,000.

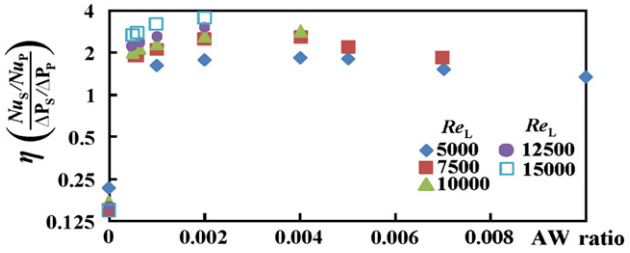

Fig. 11. Variations of η index against AW ratio at $Re_L = 5000$, 7500, 10,000, 12,500, 15,000.

insert for the air–water flows are disclosed by viewing the varying manners of $\overline{Nu}_S/\overline{Nu}_P$ against AW ratio as showed in Fig. 10, which reflect the Re_L and AW impacts on the interfacial structures that differently affect the wall-to-fluid heat transfer properties for plain and swirl tubes. Unlike the single phase flow conditions where the swirling flows induced by the spiky twisted tape play the predominant role for HTE performances, the additional manifesting HTE mechanisms in association with the two-phase phenomena develop in both plain and swirl tubes. As the HTE impacts added by the air–water two-phase flows are phenomenal in both the plain and swirl tubes, the dominant role of swirling flows for HTE impacts at the single-phase flow conditions are relatively weakened. As a result, the $\overline{Nu}_S/\overline{Nu}_P$ ratios, which are indicative of the heat transfer modifications brought by the twisted-tape insert, undergo considerable drops when the flow structures transit from the single-phase to two-phase conditions for all Re_L tested as seen in Fig. 10. Considering the flow images that indicate the Re_L and AW impacts on the interfacial structures in the plain and swirl tubes as typified in Fig. 2 while the AW impacts on $\overline{Nu}_S/\overline{Nu}_P$ in Fig. 10 are examined, the increase of Re_L at the present two-phase flow conditions consistently elevate the HTE impacts in terms of $\overline{Nu}_S/\overline{Nu}_P$ ratios for a fixed AW ratio. Such reverse Re_L impacts on $\overline{Nu}_S/\overline{Nu}_P$ for two-phase flows from the single-phase conditions are attributed to the different interfacial and near-wall flow structures between the plain and swirl tubes that differentiate the value and varying-trend of B exponents in the correlations of $\overline{Nu}_S$ and $\overline{Nu}_P$. With air–water two-phase flows, the higher B exponents in $\overline{Nu}_S$ correlations than those in $\overline{Nu}_P$ correlations cause the consistent $\overline{Nu}_S/\overline{Nu}_P$ increase as Re_L increases; while the AW-driven $\overline{Nu}_S/\overline{Nu}_P$ variations as shown in Fig. 10 are the competitive results between the AW impacts on A coefficients and B exponents. As AW ratio increases, $\overline{Nu}_S/\overline{Nu}_P$ ratios at each tested Re_L asymptotically increases after the considerable drop through the single-phase to two-phase transition as depicted by Fig. 10. Although $\overline{Nu}_P$ at the flow conditions with air–water bubbly flows are augmented considerably from the single-phase (AW = 0) $\overline{Nu}_P$ levels as seen in Fig. 7a, the results demonstrated by Fig. 10 confirm that the spiky twisted-tape insert can provide further HTE effects at the two-phase flow conditions with the HTE effectiveness enhanced by increasing Re_L. Indeed, although the reference $\overline{Nu}_P$ datum at the air–water two-phase conditions are considerably elevated from the single-phase $\overline{Nu}_P$ levels, the $\overline{Nu}_S/\overline{Nu}_P$ ratios with two-phase conditions at $Re_L = 15{,}000$ as seen in Fig. 10 have reached the single-phase (AW = 0) $\overline{Nu}_S/\overline{Nu}_P$ level. In view of the HTE impacts, the present spiky twisted-tape insert is more suitable for applications with high Re_L.

The HTE impacts offered by the spiky twisted tape in the swirl tube as depicted in Fig. 10 are generated with the expense of increased pressure drops. For the present two-phase flow conditions, the overall assessments for the relative HTE impacts and pressure-drop augmentations are performed by examining the performance index (η) defined as $((\overline{Nu}_S/\overline{Nu}_P)/(\Delta P_S/\Delta P_P)$. The previous illustrations have demonstrated that the presence of two-phase air–water flow features has neutralized the effects of the twisted-tape insert on both $\overline{Nu}_S/\overline{Nu}_P$ and $\Delta P_S/\Delta P_P$ form the single-phase conditions. As the friction and pressure drags among the interfacial air–water structures in both the plain and swirl tubes play the predominant roles for the overall pressure drop across each test tube, the additional pressure drop penalties added by the twisted-tape insert are significantly neutralized from the total pressure drop across the plain and swirl tubes with two-phase air–water flows. As a result, the thermal performance index for each two-phase flow condition examined here is significantly increased from the single-phase condition as compared in Fig. 11 where the variations of η against AW ratio at each tested Re_L are displayed. Followed by the increased $\Delta P_S/\Delta P_P$ after AW > 0.004 as seen in Fig. 4c and the $\overline{Nu}_S/\overline{Nu}_P$ date trends depicted by Fig. 10, each Re_L controlled η data-series collected in Fig. 11 shows a general varying pattern with the initial η increase to a maximum value after which the gradual η decay is subsequently followed when AW ratio is systematically increased. As seen in Fig. 11, the optimal η indices for all the Re_L tested tend to occur at about AW = 0.002. It is also noticed that, to comply with the aforementioned HTE performances attributed from the twisted tape insert, the η indices at each fixed AW ratio consistently increase with the increase of Re_L. For the present two-phase flow conditions studied, the spiky twisted-tape insert is proven as an effective HTE measure for augmenting wall-to-fluid heat transfer performances due to the further heat transfer elevations from the plain tube references and the increased η indices from the single-phase conditions. This type of HTE device for improving the thermal performances of the gas–liquid two-phase bubbly flows appears to be more effective at high Re_L conditions within the present Re_L rang tested as both $\overline{Nu}_S/\overline{Nu}_P$ and η index increase consistently as Re_L increases.

4. Conclusions

With the flow pattern controlled as the bubbly flow in the plain tube using the computerized on-line high-speed photography, this experimental study investigates the influences of a spiky twisted-tape insert on the thermal fluid performances of the tubular air–water two-phase flows with $5000 \le Re_L \le 15{,}000$ and $0.0004 \le AW \le 0.01$. In addition to the combined improvements in HTE and thermal performance factors for single-phase tubular flows [15], this type of spiky twisted tape has also proven as an effective HTE measure for improving wall-to-fluid heat transfer properties and η indices for the bubbly air–water two-phase flows. Several concluding remarks summarized as follows are emerged through this study.

1. With the presence of the spiky twisted-tape insert, the centrifugal forces induce radial segregating effect that drives the liquid-phase fluid toward tube wall with the tube core occupied by the

gas-phase fluid. Air bubbles in the swirl tube are drifting within the swirls and concentrated in the core region to enhance collisions and coalescences of bubbles with the radial α distribution as the core-peaking profile. Although the differential phase distributions and interfacial structures between the plain and swirl tubes with air–water flows are observed, the averaged void fractions across both plain and swirl tubes can be well correlated using the drift flux model by equation (1).

2. With two-phase flows, the additional frictional, accelerational and form drags, which prevail over the air–water interfacial structures play the predominant role over the wall drags in both plain and swirl tubes. Substantial increases in pressure drops from the single-phase conditions are observed in both plain and swirl tube. But the relative pressure-drop increases by inserting the spiky twisted-tape for two-phase flows, indexed by $\Delta P_S/\Delta P_P$, are significantly reduced from single-phase levels as the impacts of the additional wall-drags induced by the twisted-tape are neutralized as the predominant drags develop among the air–water interfacial structures.
3. The spiky twisted tape insert induces swirls and trips numerous separated shear layers behind these spikes along the swirl tube, which interact together to promote heat transfer performances for the single-phase flows with Nu_S/Nu_P raising to the range of 2.75–3.25. With the presence of the agitated air-bubbles to augment local mass/heat flux exchanges in both plain and swirl tubes, local Nu_P and Nu_S are consistently increased as AW ratio increases from the AW = 0 condition for each Re_L tested. Because such AW-driven Nu_P and Nu_S elevations are amplified as Re_L increases, the interdependent Re_L and AW effects exist in Nu_P and Nu_S correlations. Justified by the data trends revealed in Figs. 7 and 8, the $\overline{Nu}_P$ and $\overline{Nu}_P$ correlations are derived as equations (2) and (3) that respectively permit the evaluation of the interdependent and individual Re_L and AW impacts on the heat transfer levels over the developed flow region for the tubular air–water bubbly flows without and with the spiky twisted tape insert.
4. As Re_L increases at AW = 0 conditions, $\overline{Nu}_S/\overline{Nu}_P$ consistently drops, indicating the weakened HTE impacts at high Reynolds numbers for single phase flows. Due to the additional manifesting HTE mechanisms in association with the two-phase phenomena in both plain and swirl tubes, the dominancy of swirls for HTE impacts are relatively weakened so that the $\overline{Nu}_S/\overline{Nu}_P$ ratios drop considerably after the flow transits from the single-phase to two-phase flows. However, due to the different interfacial and near-wall flow structures between the plain and swirl tubes that differentiate B exponents in $\overline{Nu}_S$ and $\overline{Nu}_P$ correlations, the increase of Re_L consistently elevate $\overline{Nu}_S/\overline{Nu}_P$ ratios for a fixed AW ratio. It is demonstrated that the present spiky twisted-tape can provide further HTE effects at the two-phase flow conditions with the HTE effectiveness enhanced by increasing Re_L.
5. While the $\overline{Nu}_S/\overline{Nu}_P$ ratios are raised to the similar ranges between the single- and two-phase flows, the presence of two-phase phenomena has neutralized the pressure-drop penalty added by the twisted-tape insert from the total pressure drop across the plain and swirl tubes with air–water flows. As a result, the thermal performance index for each two-phase flow condition is significantly increased from the single-phase level which demonstrates the effectiveness of the present spiky twisted-tape insert for improving the HTE and thermal performances of the tubular air–water bubbly flows.

Acknowledgement

This research project was financially supported by National Science Council, Taiwan, under the grant number NSC 97-2221-E-022-013-MY3.

References

[1] S. Martemianov, V.L. Okulov, On heat transfer enhancement in swirl pipe flows, Int. J. Heat Mass Transfer 47 (2004) 2379–2393.
[2] E. Smithberg, F. Landis, Friction and forced convection heat transfer characteristics in tubes with twisted tape swirl generators, ASME J. Heat Transfer 86 (1964) 39–49.
[3] R.F. Lopina, A.E. Bergles, Heat transfer and pressure drop in tape generated swirl flow, ASME J. Heat Transfer 91 (1969) 434–442.
[4] R.M. Manglik, A.E. Bergles, Heat transfer and pressure drop correlations for twisted tape inserts in isothermal tubes: part I – laminar flows, ASME J. Heat Transfer 115 (1993) 881–889.
[5] R.M. Manglik, A.E. Bergles, Heat transfer and pressure drop correlations for twisted tape inserts in isothermal tubes: part II – transition and turbulent flows, ASME J. Heat Transfer 115 (1993) 890–896.
[6] S.K. Agarwal, R.M. Raja, Heat transfer augmentation for the flow of a viscous liquid in circular tubes using twisted tape inserts, Int. J. Heat Mass Transfer 39 (1996) 3547–3557.
[7] L. Wang, B. Sundén, Performance comparison of some tube inserts, Int. Comm. Heat Mass Transfer 29 (2002) 45–56.
[8] P.K. Sarma, P.S. Kishore, R.V. Dharma, T. Subrahmanyam, A combined approach to predict friction coefficients and convective heat transfer characteristics in a tube with twisted tape inserts for a wide range of *Re* and *Pr*, Int. J. Thermal Sciences 44 (2005) 393–398.
[9] S.W. Chang, Y. Zheng, Enhanced heat transfer with swirl duct under rolling and pitching environment, J. Ship Res. 46 (2002) 149–166.
[10] S. Ray, A.W. Date, Friction and heat transfer characteristics of flow through square duct with twisted tape insert, Int. J. Heat Mass Transfer 46 (2003) 889–902.
[11] Q. Liau, M.D. Xin, Augmentation of convective heat transfer inside tubes with three-dimensional internal extended surfaces and twisted tape inserts, Chem. Eng. J. 78 (2000) 95–105.
[12] V. Zimparov, Enhancement of heat transfer by a combination of three-start spirally corrugated tubes with a twisted tape, Int. J. Heat Mass Transfer 44 (2001) 551–574.
[13] V. Zimparov, Enhancement of heat transfer by a combination of a single start spirally corrugated tubes with a twisted tape, Exp. Thermal Fluid Sci. 25 (2002) 535–546.
[14] S.W. Chang, Y.J. Jan, J.S. Liou, Turbulent heat transfer and pressure drop in tube fitted with serrated twisted-tape, Int. J. Thermal Sci. 46 (2007) 506–518.
[15] S.W. Chang, T.L. Yang, J.S. Liou, Heat transfer and pressure drop in tube with broken twisted tape insert, Int. J. Exp. Thermal Fluid Sci. 32 (2007) 489–501.
[16] G. Kocamustafaogullari, W.D. Huang, J. Razi, Measurement of modeling of average void fraction, bubble size and interfacial area, Nucl. Eng. Design 148 (1994) 437–453.
[17] T. Hibiki, M. Ishii, Experimental study on interfacial area transport in bubbly two-phase flows, Int. J. Heat Mass Transfer 42 (1999) 3019–3035.
[18] I. Zun, I. Kljenak, S. Moze, Space-time evolution of the nonhomogeneous bubble distribution in upward flow, Int. J. Multipass Flow 19 (1993) 151–172.
[19] A. Ohnuki, H. Akimoto, Experimental study on transition of flow pattern and phase distribution in upward air–water two-phase flow along a large vertical pipe, Int. J. Multiphase Flow 26 (2000) 367–386.
[20] S. Guet, G. Ooms, R.V.A. Oliemans, Influence of bubble size on the transition from low-Re bubbly flow to slug flow in a vertical pipe, Exp. Thermal Fluid Sci. 26 (2002) 635–641.
[21] T. Hibiki, M. Ishii, Interfacial area concentration in steady fully-developed bubbly flow, Int. J. Heat Mass Transfer 44 (2001) 3443–3461.
[22] H.Y. Kim, S. Koyama, W. Matsumoto, Flow pattern and flow characteristics for counter-current two-phase flow in a vertical round tube with wire-coil inserts, Int. J. Multiphase Flow 27 (2001) 2063–2081.
[23] V.V. Yahov, Heat transfer and crisis in swirl flow boiling, Exp. Thermal Fluid Sci. 29 (2005) 871–883.
[24] Y. Murai, S. Yoshikawa, S. Toda, M. Ishikawa, F. Yamamoto, Structure of air–water two-phase flow in helically coiled tubes, Nucl. Eng. Design 236 (2006) 94–106.
[25] A.E. Bergles, W.D. Fuller, S.J. Hynek, Dispersed flow film boiling of nitrogen with swirl flow, Int. J. Heat Mass transfer 14 (9) (1971) 1343–1354.
[26] Editorial Board of ASME Journal of Heat Transfer, Journal of heat transfer policy on reporting uncertainties in experimental measurements and results, ASME J. Heat Transfer 115 (1993) 5–6.
[27] T. Hibiki, M. Ishii, One-group interfacial area transport of bubbly flows in vertical round tubes, Int. J. Heat Mass Transfer 43 (2000) 2711–2726.
[28] R. Rozenblit, M. Gurevich, Y. Lengel, G. Hetsroni, Flow patterns and heat transfer in vertical upward air–water flow with surfactant, Int. J. Multiphase Flow 32 (2006) 889–901.
[29] F.W. Dittus, L.M.K. Boelter, University of California, Berkeley, CA, Publications in Engineering 2 (1930) 443.7.
[30] G.E. Thorncroft, J.F. Klausner, R. Mei, An experimental investigation of bubble growth and detachment in vertical upflow and downflow boiling, Int. J. Heat Mass Transfer 41 (1998) 3857–3871.